Opto-Electronic Advances

CN 51–1781/TN ISSN 2096–4579 (Print) ISSN 2097–3993 (Online)

Multi-prior physics-enhanced neural network enables pixel super-resolution and twin-image-free phase retrieval from single-shot hologram

Xuan Tian, Runze Li, Tong Peng, Yuge Xue, Junwei Min, Xing Li, Chen Bai and Baoli Yao

Citation: Tian X, Li RZ, Peng T, et al. Multi-prior physics-enhanced neural network enables pixel super-resolution and twin-image-free phase retrieval from single-shot hologram. *Opto-Electron Adv* **7**, 240060(2024).

https://doi.org/10.29026/oea.2024.240060

Received: 14 March 2024; Accepted: 1 July 2024; Published online: 28 August 2024

Related articles

Large-field objective lens for multi-wavelength microscopy at mesoscale and submicron resolution

Xin Xu, Qin Luo, Jixiang Wang, Yahui Song, Hong Ye, Xin Zhang, Yi He, Minxuan Sun, Ruobing Zhang, Guohua Shi

Opto-Electronic Advances 2024 **7**, 230212 doi: 10.29026/oea.2024.230212

Multiplexed stimulated emission depletion nanoscopy (mSTED) for 5-color live-cell long-term imaging of organelle interactome

Yuran Huang, Zhimin Zhang, Wenli Tao, Yunfei Wei, Liang Xu, Wenwen Gong, Jiaqiang Zhou, Liangcai Cao, Yong Liu, Yubing Han, Cuifang Kuang, Xu Liu

Opto-Electronic Advances 2024 **7**, 240035 doi: 10.29026/oea.2024.240035

Improved spatiotemporal resolution of anti-scattering super-resolution label-free microscopy via synthetic wave 3D metalens imaging

Yuting Xiao, Lianwei Chen, Mingbo Pu, Mingfeng Xu, Qi Zhang, Yinghui Guo, Tianqu Chen, Xiangang Luo

Opto-Electronic Science 2023 **2**, 230037 doi: 10.29026/oes.2023.230037

More related article in Opto-Electronic Journals Group website

Opto-Electronic Advances

Article

September 2024, Vol. 7, No. 9

DOI: 10.29026/oea.2024.240060

Multi-prior physics-enhanced neural network enables pixel super-resolution and twin-image-free phase retrieval from single-shot hologram

Xuan Tian[1,2†], Runze Li[1†], Tong Peng[1], Yuge Xue[1,2], Junwei Min[1], Xing Li[1], Chen Bai[1,2*] and Baoli Yao[1,2*]

Digital in-line holographic microscopy (DIHM) is a widely used interference technique for real-time reconstruction of living cells' morphological information with large space-bandwidth product and compact setup. However, the need for a larger pixel size of detector to improve imaging photosensitivity, field-of-view, and signal-to-noise ratio often leads to the loss of sub-pixel information and limited pixel resolution. Additionally, the twin-image appearing in the reconstruction severely degrades the quality of the reconstructed image. The deep learning (DL) approach has emerged as a powerful tool for phase retrieval in DIHM, effectively addressing these challenges. However, most DL-based strategies are data-driven or end-to-end net approaches, suffering from excessive data dependency and limited generalization ability. Herein, a novel multi-prior physics-enhanced neural network with pixel super-resolution (MPPN-PSR) for phase retrieval of DIHM is proposed. It encapsulates the physical model prior, sparsity prior and deep image prior in an untrained deep neural network. The effectiveness and feasibility of MPPN-PSR are demonstrated by comparing it with other traditional and learning-based phase retrieval methods. With the capabilities of pixel super-resolution, twin-image elimination and high-throughput jointly from a single-shot intensity measurement, the proposed DIHM approach is expected to be widely adopted in biomedical workflow and industrial measurement.

Keywords: optical microscopy; quantitative phase imaging; digital holographic microscopy; deep learning; super-resolution

Tian X, Li RZ, Peng T et al. Multi-prior physics-enhanced neural network enables pixel super-resolution and twin-image-free phase retrieval from single-shot hologram. *Opto-Electron Adv* **7**, 240060 (2024).

Introduction

Transparent specimens exhibit minimal absorption but instead induce a phase change in light wavefronts, rendering them invisible under conventional optical microscopy. Alternatively, as an interference technique, digital holographic microscopy (DHM) has been used as a convenient approach for non-destructive phase imaging[1], DHM typically employs two major configurations: in-line and off-axis structures. The off-axis DHM allows wavefront reconstruction from a single-shot digital hologram, but suffers from the loss of space-bandwidth and the resolution[1,2]. In comparison, the digital in-line holographic microscopy (DIHM), with its relatively higher space-bandwidth product, is often preferred in some

[1]State Key Laboratory of Transient Optics and Photonics, Xi'an Institute of Optics and Precision Mechanics, Chinese Academy of Sciences, Xi'an 710119, China; [2]University of Chinese Academy of Sciences, Beijing 100049, China.

[†]These authors contributed equally to this work.

*Correspondence: C Bai, E-mail: baichen@opt.ac.cn; BL Yao, E-mail: yaobl@opt.ac.cn

Received: 14 March 2024; Accepted: 1 July 2024; Published online: 28 August 2024

microscopic scenes[3].

Unfortunately, two factors often obfuscate the high-quality reconstruction in practical DIHM, i.e., the loss of sub-pixel information and the well-known twin-image. In optical systems, detectors are typically designed with larger pixel sizes to accommodate high photosensitivity, large field-of-view (FOV), and improved signal-to-noise ratio (SNR) during limited exposure time[4]. However, the use of large pixel sizes may lead to inadequate sampling of the transmitted wavefront, resulting in low pixel resolution and the down-sampling problem[4]. Although deploying magnification camera adapters or using image sensors with smaller pixel sizes could mitigate the sub-pixel information loss problem, it comes at the cost of the reduced FOV. In terms of twin-image, as a characteristic noise that manifests itself as an out of focus version of the reconstructed plane, is commonly caused by incomplete data acquisition by digital image sensors which only contain the intensity information of the complex optical field[3]. While some holographic setups capable of eliminating the twin-image have been presented, they add complexity to the recording process, by introducing sensible optical elements or imposing new constraints, such as the resolution loss in the off-axis holography[5].

Since DIHM only depends on intensity measurement, the phase reconstruction, known as phase retrieval, can be regarded as a highly ill-conditioned inverse problem[6]. An effective way to solve this inverse problem in DIHM is to introduce additional and potential information during imaging procedure. Therefore, both of the sub-pixel information loss and the twin-image can be addressed by using diversity information from multiple holograms. For instance, the de-multiplexing algorithm could alleviate phase retrieval with loss of sub-pixel information. However, its capability is still restrained by the elaborate illumination scheme and the requirement of multiple detections[4]. Alternatively, pixel super-resolution (PSR) techniques, such as sub-pixel shifting[7] or wavelength scanning[8], utilizes observation diversity that provides extra information of the latent high-resolution image while increasing measurement noise. Besides, most existing PSR algorithms based on alternating projection (AP) techniques are not robust to noise[9,10]. The twin-image can be eliminated by record multiple holograms as well. Specifically, the twin-image-free phase distribution of a specimen can be reconstructed with the aid of multiple wavelengths[11], illumination angles[12], or phase shifts[13], though the achievable imaging resolution is restricted to the incoherent diffraction limit. Nevertheless, the acquisition of multiple holograms often leads to increased experimental complexity and elevated system costs, as well as poor image acquisition rate.

High-throughput and high-accuracy phase retrieval without sacrificing FOV or requiring additional hardware is more practical for observing live samples. Instead of using multiple holograms, a strategy for solving the inverse problem of phase imaging is to integrate the known prior information into computational methods to obtain high-accuracy phase imaging from a single hologram. A classic approach is to introduce sparse priors in PSR reconstruction[14], but this often lacks robustness to deviations in the nominal parameters of the system. In contrast, using a trained denoiser as a prior has led to the development of modified plug-and-play optimization for PSR phase retrieval (PnP-PSR) based on the AP framework[10]. However, it cannot cope well with intense noise. To reduce twin-image influence, combining the Gerchberg-Saxton (GS) algorithm[15] with the known amplitude distribution of the incident light field demonstrates the advantage of requiring only a single hologram for phase retrieval. Additionally, physics-driven compressive sensing-digital holography (CS-DH)[16] based on Fourier analysis and sparsity achieves high accuracy, but it requires exact estimation of backward propagation for optical imaging. These strategies are generally limited as they require perfectly tuned parameters, and are difficult to implement in the presence of strong noise due to using a single prior. When sub-pixel information is lost, the twin-image and noise will become more pronounced due to ill-posed phase retrieval[17].

Recently, the deep learning (DL) network has been proven to be a powerful tool for phase retrieval with unprecedented performance[18,19]. It eliminates the need for tedious image acquisition process and time-consuming iterations, while maintaining high-quality reconstructed phase images. A DL-based pixel-super-resolved quantitative phase microscopy has been proposed by training a neural network with paired low-resolution intensity and high-resolution phase data. This approach is well-suited for live cell imaging and enables high-throughput long-term dynamic phase reconstruction[4]. In addition, DL has also been successfully applied to artifacts-free or twin-image-free phase retrieval[19]. However, most DL-based strategies are data-driven or end-to-end net approaches, suffering from excessive data dependency and limited generalization ability. In contrast, a training-free DL

approach combines a complete physical model representing the imaging process with the deep image prior (DIP)[20] frame to solve the phase retrieval issues[6,21]. These paradigms allow direct learning of high-dimensional representations from captured data using untrained neural networks based on physical models, i.e. physics-enhanced network (PN), making them more practically interpretable. Nevertheless, it has been found that directly applying the DIP framework with a single prior to solve ill-posed inverse problems often leads to pseudo-solution[22] or overfitting of interference-related noise and weight decay[23]. Moreover, to our knowledge, High-throughput quantitative phase imaging with both pixel super-resolution and twin-image-free from hologram in DIHM has not been realized yet.

In this work, a multi-prior physics-enhanced neural network with PSR (MPPN-PSR) that encapsulates the physical model prior, sparsity prior and deep image prior within an untrained deep neural network has been proposed. The physical model priors represent the DIHM imaging process and detector down-sampling, while the sparsity prior further enhances the imaging resolution. Consequently, the retrieval of phase distribution can be achieved with pixel super-resolution, twin-image-free, and insensitivity to noise without any additional hardware design. MPPN-PSR improves the space-bandwidth product (SBP) since the inherent large FOV of the low-resolution intensity image is exploited. In addition, MPPN-PSR maximizes the data efficiency by reducing the intensity image redundancy requirement to only one frame, and the phase reconstruction speed is greatly accelerated by utilizing the graphics processing unit (GPU). The performance and effectiveness of MPPN-PSR was evaluated by comparing with other retrieval methods through both simulations and experiments. Given its capability of achieving pixel super-resolution, twin-image elimination and large-SBP phase reconstruction, we provide high-throughput phase images with high accuracy. These superior performances indicate that the proposed approach is a promising tool to be widely adopted in biomedical workflow and industrial measurement.

Methods

Problem statement and reconstruction methods

When an object with the phase distribution of $\boldsymbol{\Psi}(z=0)$ is illuminated by coherent plane waves, the output complex amplitude $\boldsymbol{U}_0$ can be expressed as:

$$\boldsymbol{U}_0\left(z=0\right)=\exp\left[\mathrm{i}\boldsymbol{\Psi}\left(z=0\right)\right]. \tag{1}$$

The diffraction pattern $\boldsymbol{U}_z(z=d)$ with a propagation distance $z=d$ is given as follows:

$$\begin{aligned}\boldsymbol{U}_z\left(z=d\right)&=\iint\hat{\boldsymbol{U}}_0\left(f_x,f_y\right)\boldsymbol{M}\exp\left[\mathrm{i}2\pi\left(f_x,f_y\right)\right]\mathrm{d}f_x\mathrm{d}f_y\\&=\boldsymbol{P}\left[\boldsymbol{\Psi}\left(z=0\right)\right],\end{aligned} \tag{2}$$

where $\boldsymbol{M}=\exp\left(\mathrm{i}kz\sqrt{1-\left(\lambda f_x\right)^2-\left(\lambda f_y\right)^2}\right)$ is the transfer function, $\hat{\boldsymbol{U}}_0$ is the 2D Fourier transform of $\boldsymbol{U}_0$, f_x and f_y are the spatial frequency coordinates, and $\boldsymbol{P}$ is a transform operator expressing from $\boldsymbol{\Psi}(z=0)$ to $\boldsymbol{U}_z(z=d)$. Because the image sensor only responds to the light intensity, and the large pixel size of the sensor also results in down-sampling, the complete mapping from the object phase to the hologram recorded by the sensor can be expressed as follows:

$$\begin{aligned}\boldsymbol{I}\left(z=d;\theta\right)&=\boldsymbol{D}_\theta\left\{\left|\boldsymbol{U}_z\left(z=d\right)\right|^2\right\}\\&=\boldsymbol{D}_\theta\left\{\left|\boldsymbol{P}\left[\boldsymbol{\Psi}\left(z=0\right)\right]\right|^2\right\}\\&=\boldsymbol{F}_\theta\left\{\boldsymbol{\Psi}\right\},\end{aligned} \tag{3}$$

where $\boldsymbol{D}_\theta\{\cdot\}$ represents down-sampling process with the rate of θ, and $\boldsymbol{F}_\theta\{\cdot\}$ is the mapping function relates the phase object $\boldsymbol{\Psi}$ to the measured diffraction pattern $\boldsymbol{I}$. It should be noted that the mapping function is ill-posed, since information recorded by the sensor is incomplete due to the intensity response and limited pixel size of sensor. The objective of the phase retrieval problem is to formulate an inverse mapping $\boldsymbol{F}_\theta^{-1}\{\cdot\}$:

$$\boldsymbol{\Psi}\left(z=0\right)=\boldsymbol{F}_\theta^{-1}\left\{\boldsymbol{I}\left(z=d;\theta\right)\right\}. \tag{4}$$

Most existing iterative algorithms for solving the inverse problem are single-task, i.e., their forward models are established as $\boldsymbol{F}_{\text{twin-image}}=\left|\boldsymbol{U}_z(z=d)\right|^2+\boldsymbol{E}$ or $\boldsymbol{F}_{\text{down-sampling}}=\boldsymbol{D}_\theta\{\boldsymbol{I}\}+\boldsymbol{E}$, where $\boldsymbol{E}$ is the noise term. In other words, such approaches solely focus on twin-image suppression or pixel super-resolution, rather than dealing with both tasks, such as the physics-driven CS-DH[16] or the PnP-PSR[10] mentioned above. Joint processing of sub-pixel information loss and twin-images is a challenge. Specifically, when the image processes of down-sampling and twin-image generating are combined in a forward model as Eq. (3), the typical approach of the inverse problem is to solve minimization as:

$$\hat{\boldsymbol{\Psi}}=\underset{\boldsymbol{\Psi}}{\operatorname{argmin}}\left\{\left\|\boldsymbol{I}-\boldsymbol{F}_\theta\boldsymbol{\Psi}\right\|_2^2+R\left(\boldsymbol{\Psi}\right)\right\}, \tag{5}$$

where $R(\boldsymbol{\Psi})$ is handcrafted or dictionary prior that can

capture the general regularity of the object $\hat{\boldsymbol{\Psi}}$. As shown in Fig. 1(a), this minimizing problem can be naturally considered as a simple way that imposes a sparsity constraint, e.g., applying total variation (TV) on a classical iterative solver such as two-step iterative shrinkage/thresholding (TwIST) to form the TwIST-TV-based approach. However, due to the limited discriminative power of handcrafted priors[23], iterative methods often fail to capture the rich structure of samples and are challenging to converge when meeting the synthesis problem of down-sampling, twin-image and intense noise, which should be proved in the subsequent sections. Another common problem of this class of methods is exact estimation of the inverse mapping $\boldsymbol{F}_\theta^{-1}\{\cdot\}$ and perfectly tuned parameters are required[24].

On the other hand, deep learning has been proven to reconstructing phase robustly. Typical DL-based methods try to learn the mapping function of the neural network $\boldsymbol{G}^p_{\text{typical}}$ from a large number of labeled data training set $S_\text{T} = \{(\boldsymbol{\Psi}_q, \boldsymbol{I}_q), q = 1,2,\cdots,Q\}$ by:

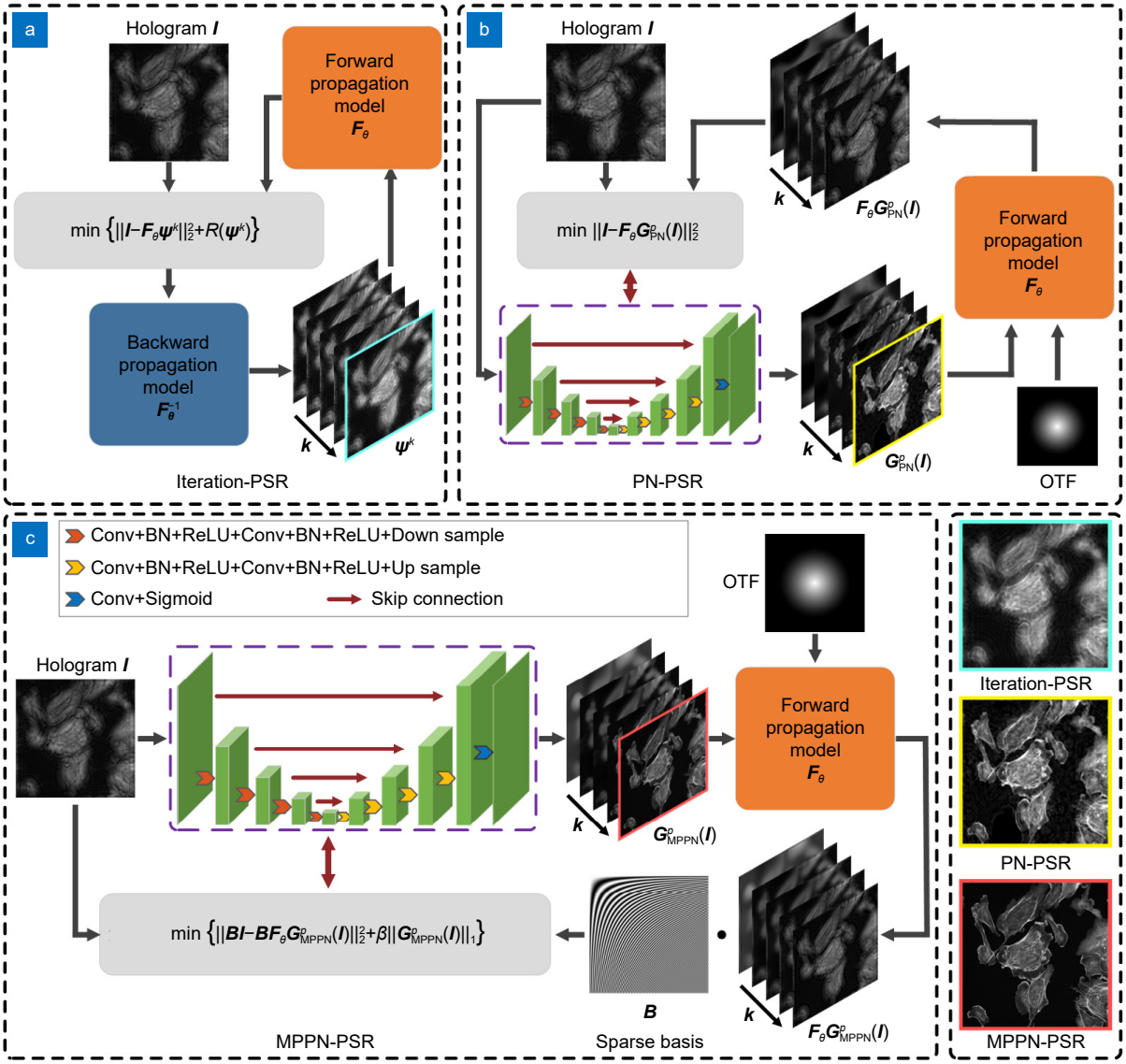

Fig. 1 | An overview of the proposed reconstruction method. (**a**) Diagrams of classical solutions based on CS and TV regularization framework. (**b**) DIP-based reconstruction method combined with physical model. (**c**) Pipeline of MPPN-PSR for hologram reconstruction. A measured hologram $\boldsymbol{I}$ of a phase object $\boldsymbol{\Psi}$ is the input to the neural networks. The output of the neural networks is taken as the estimated phase $\boldsymbol{G}^p_{\text{MPPN}}(\boldsymbol{I})$, which is then numerically propagated to simulate the diffraction and measurement processes $\boldsymbol{F}_\theta$ to generate $\boldsymbol{F}_\theta\boldsymbol{G}^p_{\text{MPPN}}(\boldsymbol{I})$. The sparsity prior $\boldsymbol{B}$ additionally enhances the imaging resolution. The mean square errors (MSEs) between $\boldsymbol{BI}$ and $\boldsymbol{BF}_\theta\boldsymbol{G}^p_{\text{MPPN}}(\boldsymbol{I})$ are measured as the loss value to adjust the neural network parameters.

$$\boldsymbol{G}^{p}_{\text{typical}} = \underset{p\in\Theta}{\operatorname{argmin}} \left\| \boldsymbol{G}^{p}_{\text{typical}}(\boldsymbol{I}_q) - \boldsymbol{\Psi}_q \right\|_2^2, \forall(\boldsymbol{I}_q, \boldsymbol{\Psi}_q) \in S_T \,, \tag{6}$$

where $\boldsymbol{G}^{p}_{\text{typical}}$ is defined by a set of weights and biases $p\in\Theta$. The performance of $\boldsymbol{G}^{p}_{\text{typical}}$ is heavily dependent on the size and variance of training set, which can often be thousands or even larger. In a typical DL application, the size of training set can be thousands or even larger, to produce feasible mapping function between the hologram and the corresponding phase through a training process[21]. It is experimentally time-consuming to collect such a large group of holograms and their corresponding original phase. In addition, only the object set with the same priority used in the training process can obtain good generalization effect[21]. In contrast, the ground-truth phase explicitly does not appear in the objective function of PN-based approaches, meaning that such type of method does not require the ground-truth phase for training. Instead, it is the interplay between forward mode $\boldsymbol{F}_\theta$ and the parameters of the network $\boldsymbol{G}^{p}_{\text{PN}}$ that causes the prior of the measured diffraction pattern $\boldsymbol{I}$ to be captured by the handcrafted neural network[6,21]. As shown in Fig. 1(b), a complete physical model is integrated with a neural network to solve the reconstruction issues of DIHM, which can be formulated as:

$$\boldsymbol{G}^{p}_{\text{PN}} = \underset{p\in\Theta}{\operatorname{argmin}} \left\| \boldsymbol{I} - \boldsymbol{F}_\theta \boldsymbol{G}^{p}_{\text{PN}}(\boldsymbol{I}) \right\|_2^2 \,. \tag{7}$$

In this objective function, the PN-PSR approach does not need to be trained in the basic truth stage. Alternatively, the error between the estimated and the measured hologram is fed back to update the parameters of the network. After optimization, the phase can be expectedly reconstructed using the obtained mapping function $\boldsymbol{G}^{p}_{\text{PN}}$ as $\boldsymbol{\Psi}(z=0)=\boldsymbol{G}^{p}_{\text{PN}}[\boldsymbol{I}(z=d;\theta)]$. However, when using the PN-PSR framework to solve inverse problem that map from low dimensions to high dimensions, inversion results tend to get trapped in a pseudo-solution[22], mainly because such problems are more ill-posed owing to their relatively high dimensionality and incomplete information caused by down-sampling.

In fact, sparsity has been shown to be more effective in computational imaging[25], and ℓ-1 regularization has also proven to be advantageous in super-resolution reconstruction[26]. It is reasonable to incorporate sparsity and ℓ-1 regularization into a neural network for phase retrieval from single-shot DIHM, thus forming the MPPN-PSR network method, as shown in Fig. 1(c). Besdies, since ℓ-2 loss is convex and differentiable, it can provide maximum likelihood estimation in the case of independent and identically distributed Gaussian noise, which has become the most commonly used loss function in regression problems, pattern recognition, and image processing[27]. Therefore, we used a linear combination of ℓ-2 norm and ℓ-1 norm as the loss function in our method. The optimization equation of MPPN-PSR can be expressed as:

$$\boldsymbol{G}^{p}_{\text{MPPN}} = \underset{p,\boldsymbol{\Psi}=\boldsymbol{G}^{p}_{\text{MPPN}}(\boldsymbol{I})}{\operatorname{argmin}} \left\{ \left\| \boldsymbol{B}\boldsymbol{I} - \boldsymbol{B}\boldsymbol{F}_\theta \boldsymbol{G}^{p}_{\text{MPPN}}(\boldsymbol{I}) \right\|_2^2 + \beta \left\| \boldsymbol{G}^{p}_{\text{MPPN}}(\boldsymbol{I}) \right\|_1 \right\} \,, \tag{8}$$

where $\boldsymbol{B}$ is a sparse base, which can be obtained from some transform domain (e.g., undecimated wavelet transform, discrete Fourier transform, discrete Hartley transform, discrete cosine transform, Legendre polynomial) or through dictionary learning, while β serves as a key proportional coefficient to balance the ℓ-1 norm and ℓ-2 norm terms. In this work, we select the discrete cosine transform as the sparse base $\boldsymbol{B}$ since it has been proven to have good reconstruction performance[28]. In other words, MPPN-PSR encapsulates the physical model prior, sparsity prior and deep image prior in an untrained deep neural network. By expressing the hologram sparsely using $\boldsymbol{B}$, additional sparsity and ℓ-1 regularization constraints are applied to the untrained network's captured prior information, convergence becomes easier. The optimization of the MPPN-PSR network parameters only requires initializing the forward model for convergence and self-calibration. As a consequence, the phase can be retrieved as $\boldsymbol{\Psi}(z=0)=\boldsymbol{G}^{p}_{\text{MPPN}}[\boldsymbol{I}(z=d;\theta)]$, which addresses issues such as sub-pixel information loss, twin-image and noise interference over conventional DIHM hardware. This approach enables rapid high-resolution and high-throughput quantitative phase imaging from single-shot low-resolution intensity measurements.

The U-Net architecture[29] is used in this study to predict the phase based on the input diffraction pattern, as shown in Fig. 1(c). It is worth pointing out that there is no limitation on the network architecture that can be chosen to implement MPPN. In our study, we simply adopt U-Net for universality, which has been widely used in many other studies[21]. Typically, this network structure consists of an encoder path that takes the diffraction pattern as its input, a decoder path that outputs a

predicted phase map, and skip paths in the middle. We use four main types of modules to connect the input to the output: convolution blocks (3 × 3 convolution + batch normalization + leaky ReLU), max pooling blocks (2 × 2), up-convolution blocks (3 × 3 de-convolution + batch normalization + leaky ReLU), and skip connection blocks. We use ReLU as the activation function in the output layer. The neural network is based on the PyTorch 2.0.1 platform and implemented with Python 3.9.13. An Adam optimizer with a learning rate of 0.01 is used to optimize the weights and biases. The network generally required around 3000 periods to obtain accurate estimation of the $\boldsymbol{G}^{p}_{\mathrm{MPPN}}$. All implementations were performed on a computer with an Intel Core CPU i7-10700 processor, having 64 GB of RAM along with an NVIDIA GeForce RTX4080.

Experimental setup

An DIHM system was built to verify the effectiveness of MPPN-PSR in practice, as shown in Fig. 2. A laser beam with a wavelength of 685 nm (NOVAPRO, RGB Lasersystems Inc., Germany) passes through two lenses (L1, f = 50 mm and L2, f = 100 mm) for expansion. After passing through a polarizer (P, Thorlabs Inc., USA) to ensure consistent polarization, the beam is split into an object beam and a reference beam via a non-polarizing beam splitter 1 (NPBS1, Thorlabs Inc., USA). The object beam illuminates the specimen, and then magnified by a microscopic system consisting of an objective (either a 20× objective, NA = 0.45, Nikon Inc., Japan or a 10× objective, NA = 0.25, Nikon Inc., Japan) and a tube lens L4 (f = 200 mm). The reference beam passes through a same identical objective and tube lens L3 (f = 200 mm) to ensure an equal optical path. The object and reference beam interference after the NPBS2 to form final in-line hologram recording by a sCMOS camera (ORCA-Flash4.0 LT3, Hamamatsu Photonics Inc., Japan), with the total pixels of 2048×2048 at a pixel pitch of 6.5 μm. The camera is mounted on a motorized stage (traveling range of 25 mm, displacement accuracy of 0.05 μm, KMTS25E/M, Thorlabs Inc., USA) and placed on the image plane to ensure that the target is firstly in focus. The hologram at designed diffraction propagation distance can be precisely recorded by moving the camera along the z axis. Finally, the phase can be reconstructed from the diffraction hologram recorded at a propagation distance of $z = d$ from the image plane, where the distance z is set experimentally and empirically[6].

Results and discussion

Evaluation with the simulated test dataset

Numerical simulations were first performed to verify the performance of the MPPN-PSR method. In the simulation, the noise-free single-shot DIHM imaging results were generated using a phase target with 960 × 960 pixels, as shown in Fig. 3. The simulated illumination wavelength was 685 nm, and the maximum height L of the sample was set to 620 nm. The spatial down-sampling rate was set as θ = 3, i.e., resulting in the pixel size of the obtained hologram is 320 × 320 pixels. The propagation distance $z = d$ between the image plane and detector plane was set to be 12 mm, and the detector's pixel pitch was set to 6.5 μm. In addition, the OTF of the optical imaging system is estimated using a Gaussian function $\mathrm{OTF} = \exp\left(-f_{\mathrm{r}}^{2}/2\sigma^{2}\right)$, where the σ is set as 0.2[30].

The performance of the proposed MPPN-PSR method was evaluated and compared with other retrieval methods, as shown in Fig. 4, including back propagation, compressed sensing with TV regularization (TwIST-TV-PSR), plug-and-play frameworks (PnP-TV-PSR, PnP-FFDNet-PSR), and a physically enhanced neural network (PN-PSR). It should be notable that similar to PnP-PSR approaches, all the PSR methods are obtained by making minor modifications to the original version, which integrates the forward mode $\boldsymbol{F}_{\theta}$ of the down-sampling process, in an effort to increase its PSR capability.

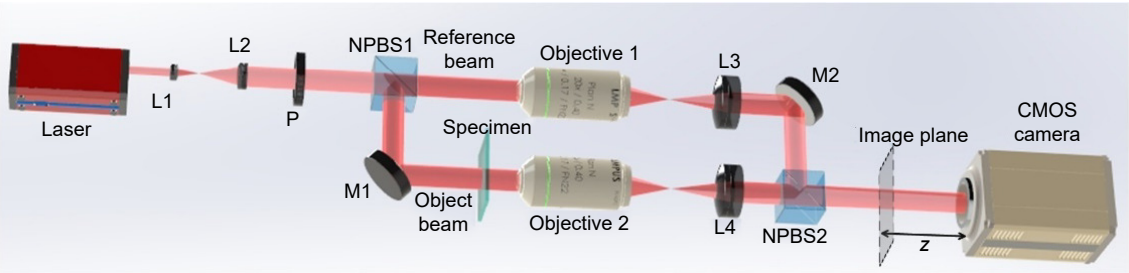

Fig. 2 | Schematic of the experimental setup of the DIHM.

Besides, all the recovery methods used are based on single-shot hologram. Intuitively, it is clearly that the reconstruction results of the proposed method are superior to others. To assess the accuracy of reconstruction, the envelopes along blue line are also investigated, in which the details provided by MPPN-PSR are closer to the ground truth. The resolution (full width at half maximum, FWHM) is measured and averaged for each lobe from the envelope of the cell in Fig. 4. Consequently, the averaged FWHM of MPPN-PSR is 10.07 μm while that of TwIST-TV-PSR is about 24.32 μm, representing that

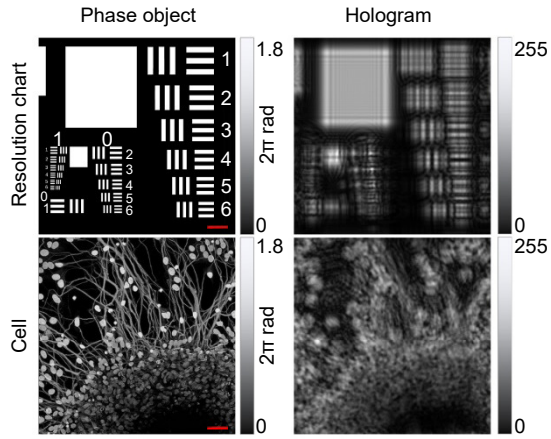

Fig. 3 | Simulated phase objects (960 × 960 pixels) and corresponding single-shot DIHM imaging results (320 × 320 pixels), in which the spatial down-sampling rate was set as θ = 3. The red scale bar measures 500 μm.

MPPN-PSR can achieve an approximate 2.4-fold increase in resolution through its embedded pixel super-resolution approach. In fact, unlike other original methods that only focus on PSR or twin-image suppression, the iterative solving strategy of inverse problem often fails to strike a balance between sub-pixel information estimation and twin-image suppression when faced with additional tasks, resulting in non-convergence and unsatisfactory results. Even though PN-PSR partially improves the reconstruction performance by encapsulating the imaging process in neural networks, its single prior mode still prevents it from meeting multitasking requirements. To quantitatively evaluate this point, the structural similarity (SSIM) and peak signal-to-noise ratio (PSNR) were used to analyze the reconstruction results, which are summarized in Table 1. The averaged PSNR and SSIM between the reconstructed phase and ground truth using MPPN-PSR are 30.86 dB and 0.90, respectively, better than the reconstruction results of other methods. In addition, the cross-section envelope can be calculated as an autocorrelation function when there is no ground truth[31], which is very useful in the quantitative analysis of experimental applications. The narrower the main lobe width of the autocorrelation function, the higher the resolution, and vice versa, the lower the resolution. To examine the effectiveness of the autocorrelation function, we investigated its consistency with the ground truth of the envelope curve in simulation, which

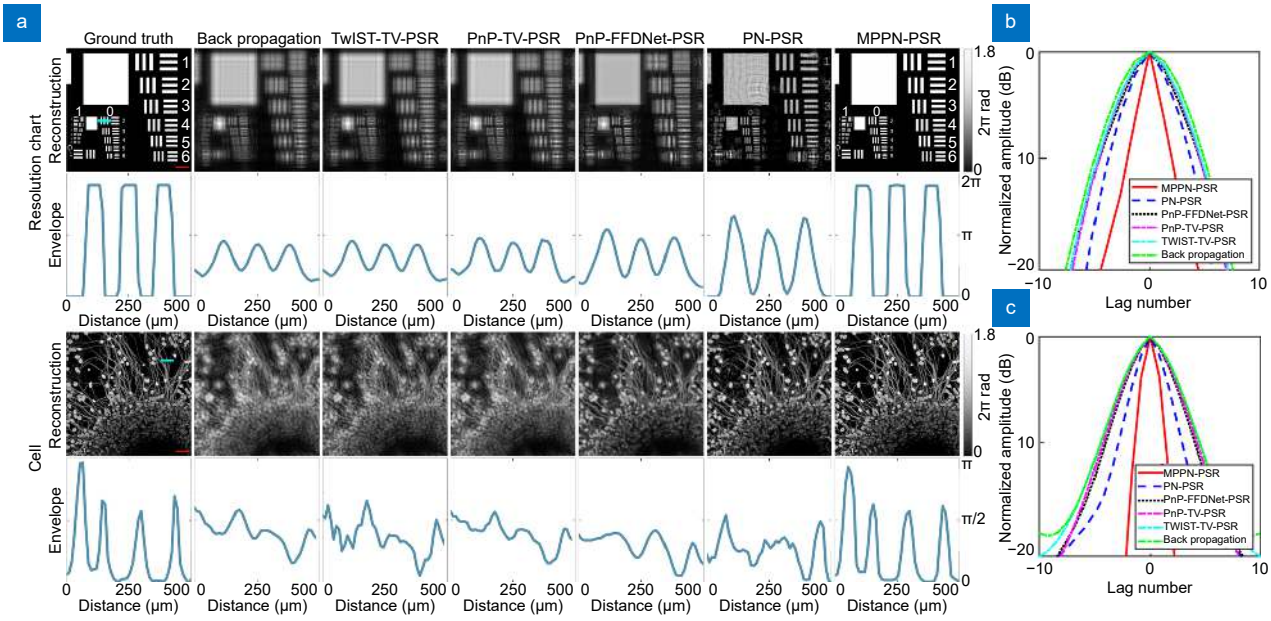

Fig. 4 | (**a**) Phase retrieval results of different methods on simulated holograms (three times down-sampling) via back propagation, TwIST-TV-PSR, PnP-TV-PSR, PnP-FFDNet-PSR, PN-PSR, and MPPN-PSR, respectively. The autocorrelation functions of (**b**) resolution chart and (**c**) cell with different methods. The profiles along the blue lines are also investigated while the red scale bar measures 500 μm.

Table 1 | Quantitative results of different methods①.

Method		Back propagation	TwIST-TV-PSR	PnP-TV-PSR	PnP-FFDNet-PSR	PN-PSR	MPPN-PSR
Resolution chart	PSNR (dB)	10.46	10.68	10.69	10.77	13.09	**36.51**
	SSIM	0.18	0.18	0.22	0.23	0.56	**0.93**
Cell	PSNR (dB)	14.41	14.93	15.27	17.66	19.26	**25.21**
	SSIM	0.29	0.37	0.37	0.39	0.61	**0.87**

①The SSIM ranges from 0 to 1 (higher is better).

is shown in Fig. 4(b) and 4(c). Specifically, the average FWHM of the main lob in the autocorrelation function of MPPN-PSR is about 2.3 times narrower than that of the TwIST-TV-PSR, which is completely consistent with the analysis of the ground truth generated by the computer.

The reconstructed results obtained from the simulated holograms with different down-sampling rates are also compared in Fig. 5. Specifically, the down-sampling rates are θ = 2, 3, and 4, corresponding to the holograms with size of 480 × 480, 320 × 320, and 240 × 240 pixels, respectively. It can be observed that, MPPN-PSR successfully reconstructs the phase from the corresponding diffraction pattern in all cases, which is consistent with the quantitative analysis shown in Table 2. On the one hand, reconstruction with an excessively high down-sampling factor introduces a significant computational burden and cause errors to a small extent. This finding further proves that resolution cannot be infinitely improved for phase reconstruction. On the other hand, even though the reconstruction performance decreases slightly as the down-sampling rate increases, MPPN-PSR still achieves convergence and produces acceptable results when θ does not exceed 4 times. Besdies, we examined the ratio β in Fig. 5(c). When β set to 1×10^{-4}, the best reconstruction performance can be achieved with a particularly typical situation at θ = 3. Indeed, this coefficient can also be slightly adjusted according to the actual imaging environment to avoid overfitting. In addition, the evolution of the MSE with an increasing number of epochs shows that the network generally required around 3000 periods to obtain accurate estimation of

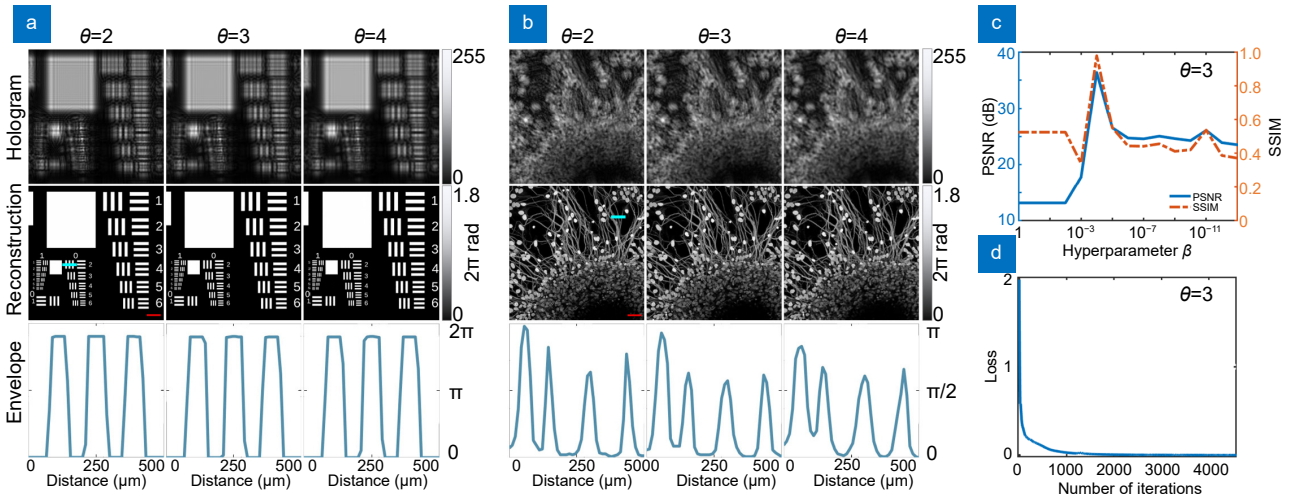

Fig. 5 | MPPN-PSR results of the holograms simulated with different down-sampling rates in terms of (**a**) resolution chart and (**b**) cell, respectively. (**c**) the examination of ratio β, which serves as a key proportional coefficient to balance the ℓ-1 norm and ℓ-2 norm terms. (**d**) The evolution of the MSE with an increasing number of epochs. The profiles along the blue lines are also investigated while the red scale bar measures 500 μm.

Table 2 | Quantitative results with the holograms simulated of different down-sampling rate.

Down-sampling rate	Resolution chart		Cell	
	PSNR (dB)	SSIM	PSNR (dB)	SSIM
θ = 2	39.12	0.94	28.59	0.91
θ = 3	36.51	0.93	25.21	0.87
θ = 4	30.10	0.89	23.10	0.83

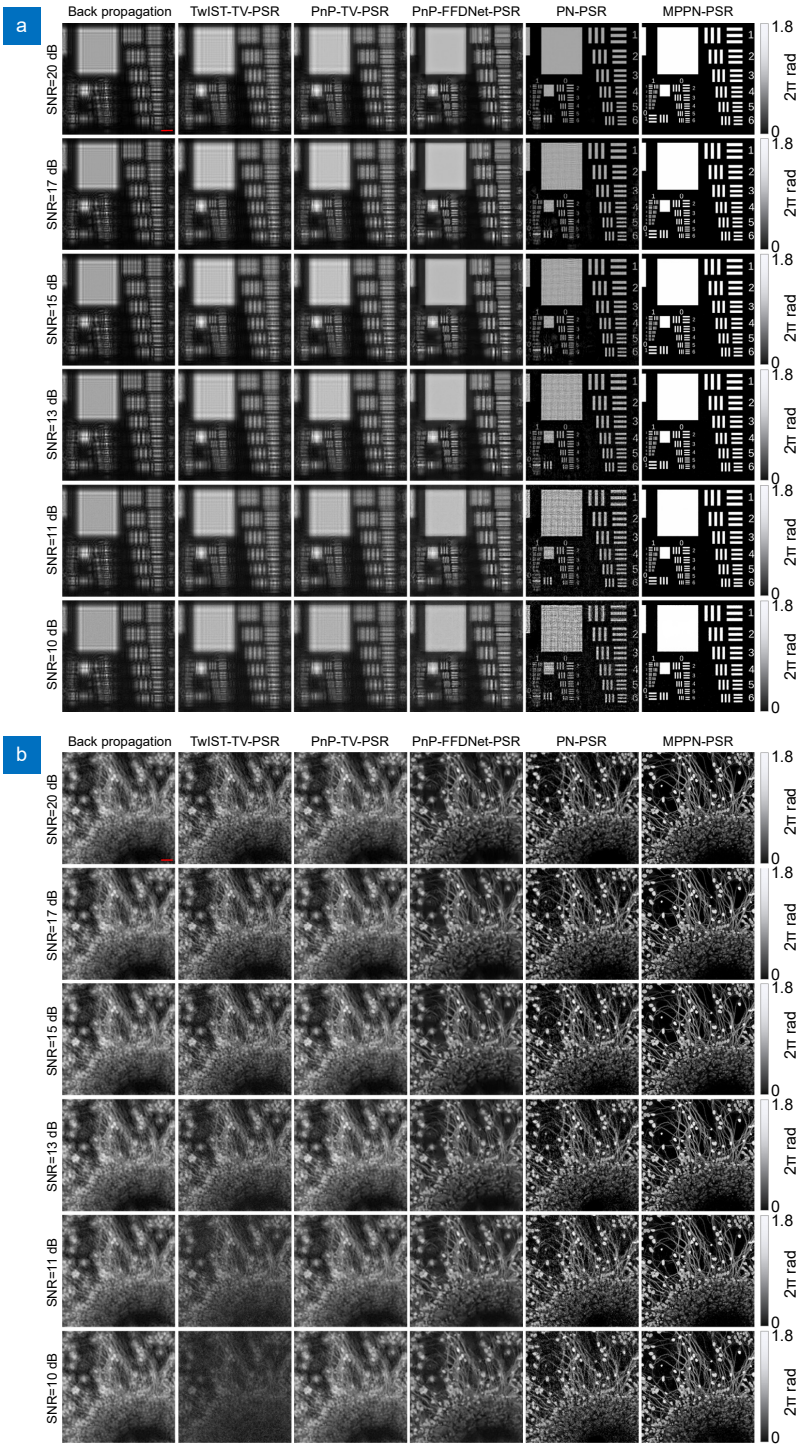

Fig. 6 | Reconstruction results of different methods at different noise levels, the red scale bar measures 500 μm. (**a**) Reconstruction results of resolution chart, the down-sampling rate $\theta = 2$. (**b**) Reconstruction results of cell, the down-sampling rate $\theta = 3$.

phase information, which can achieve a good convergence state, as shown in Fig. 5(d). The situation at $\theta = 2$ and 4 is highly similar to that at $\theta = 3$, so we will not elaborate on it here.

In addition, the noise immunity of the reconstruction is also analyzed to verify the performance of MPPN-PSR. Shot noise is added to test the robustness of these frameworks, as the model mismatch and the Poisson shot noise are the primary noise in many phase recovery applications. These can be approximated as $\boldsymbol{Y}_{\mathrm{n}} = \boldsymbol{Y}+\boldsymbol{W}$ with $\boldsymbol{W} \sim N(0, \xi\ \mathrm{Diag}(\boldsymbol{Y}))$, where $\mathrm{Diag}(\boldsymbol{Y})$ is the diagonal matrix of $\boldsymbol{Y}$, and $\boldsymbol{Y}$ is a random variable following a Poisson

distribution[6]. The reconstruction results for resolution chart and cell at different noise levels under different down-sampling rates are respectively shown in Fig. 6. Specifically, the SNR of the holograms have been reduced from 20 to 10 dB, and the down-sampling rates are set to 2 and 3, respectively. It is worth noting that due to the absence of additional sparse and regularization priors, the performance of PN-PSR witnesses a significantly decrease as the noise increases, especially in terms of SSIM. For other iterative methods, their overall imaging performance is poor due to the failure of twin-image suppression under pixel super-resolution conditions. In contrast, although the performance of MPPN-PSR slightly decreases under high-level noise as well, the quantitative analyses in Fig. 7 show that the reconstruction results are acceptable compared with other methods.

Experimental results of different samples

First, we use the standard imaging and pixel binning modes of the camera to verify the effectiveness of the proposed method. Specifically, the standard imaging mode was firstly used to capture the hologram of a quantitative phase target (USAF resolution test chart, Benchmark Technologies, USA), which is shown in Fig. 8(a), to retrieve the phase information by standard PN approach (without PSR). In this situation, the pixel size is 6.5 μm × 6.5 μm. Then, the imaging mode was switched to the BIN2×2 mode, representing the camera merges 4 pixels into one pixel output and the resolution has been reduced to 1/4 of the original. The captured hologram is shown in Fig. 8(b), where the corresponding pixel size is 13 μm × 13 μm, and the region of interest (ROI) selected by the blue box is zoomed and shown as well. In terms of the down-sampling hologram, MPPN-PSR is used for the PSR reconstruction. Compared with the reconstruction with high-sampling, MPPN-PSR has a satisfactory probability of recovering lost intermediate pixel information, which has also been verified by non-PSR reconstruction. Quantitative analysis shows that the SSIM between the two results reaches 0.897. In addition, a no-reference perceptual blur metric (NPBM)[32], ranging from 0 to 1 (lower was better) was introduced to evaluate the results due to the unavailability of the ground truth. Consequently, the NPBM of result recovered by standard imaging mode is 0.33, while that of result rebuilt by MPPN-PSR is 0.31. These all demonstrate the practicality and persuasiveness of the proposed method in application.

Then, a 620-nm-thick rectangular phase step and 20-μm-diameter polymethyl methacrylate (PMMA) beads were measured to test the feasibility and practicality of the proposed method, as shown in Fig. 9. The bright field intensity images of the samples recorded on the image plane are also shown in Fig. 9(a2) and 9(b2) for better

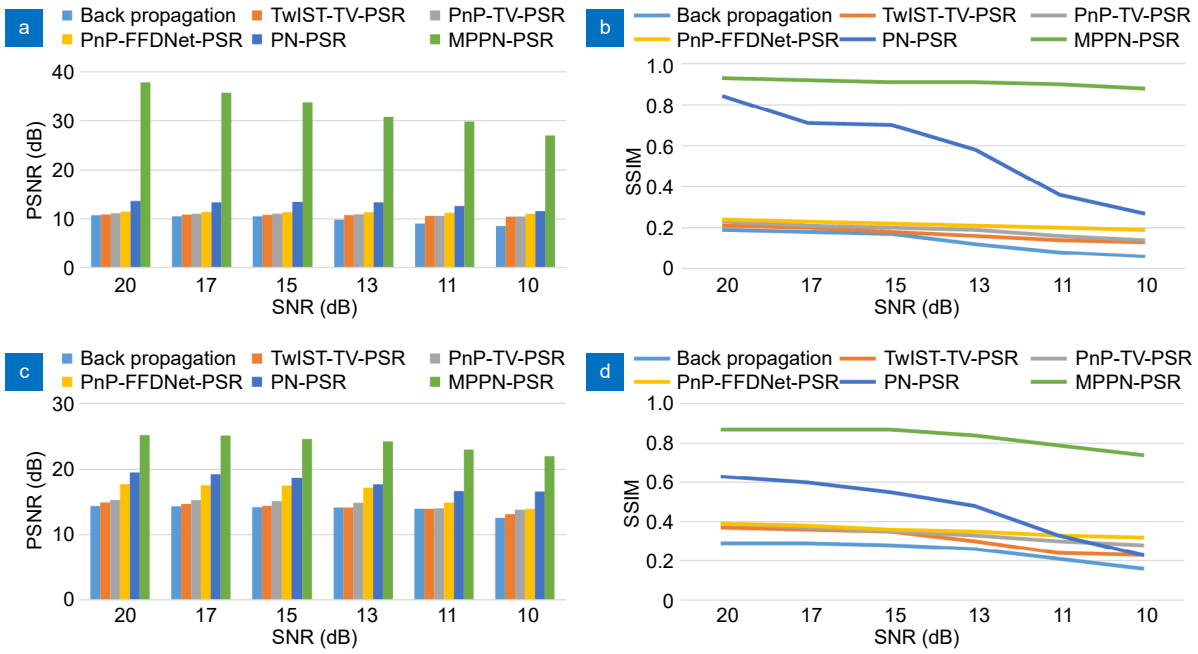

Fig. 7 | Quantitative analysis of the effect of noise on the reconstruction results using different methods. (**a**) and (**b**) are the trends of PSNR and SSIM indices of reconstruction results of resolution chart when the down-sampling rate θ = 2, while (**c**) and (**d**) are those of cell when the down-sampling rate θ = 3.

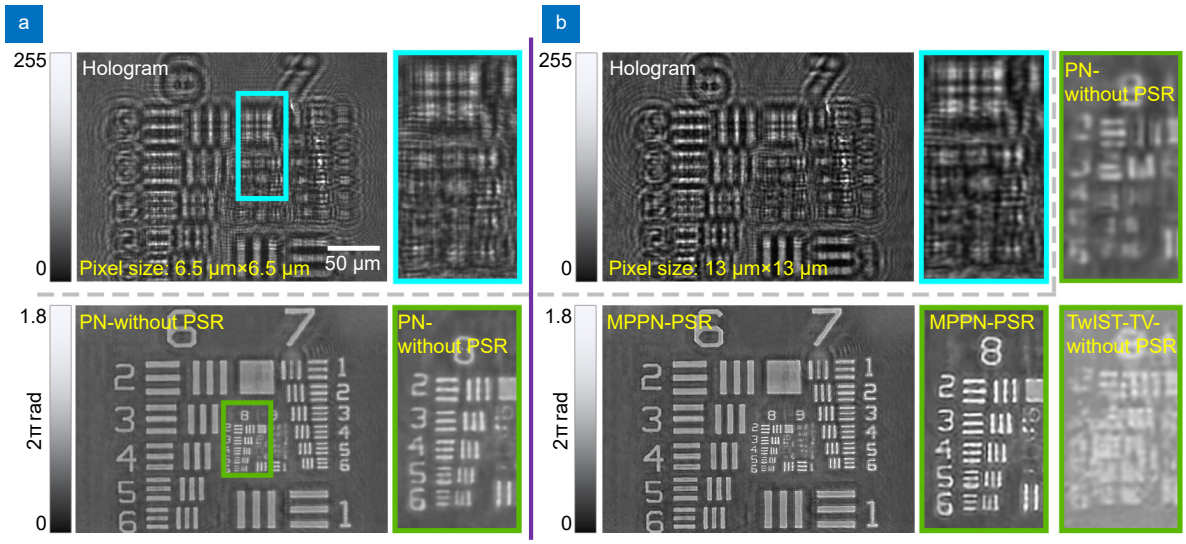

Fig. 8 | The practicality and persuasiveness of the MPPN-PSR method in real-world applications was evaluated by standard imaging and pixel binning modes of the camera. The pixel pitch varied from (**a**) 6.5 μm to (**b**) 13 μm, representing the resolution has been reduced to 1/4 of the original. The blue and green boxes respectively select the ROI of the hologram and results reconstructed by different methods.

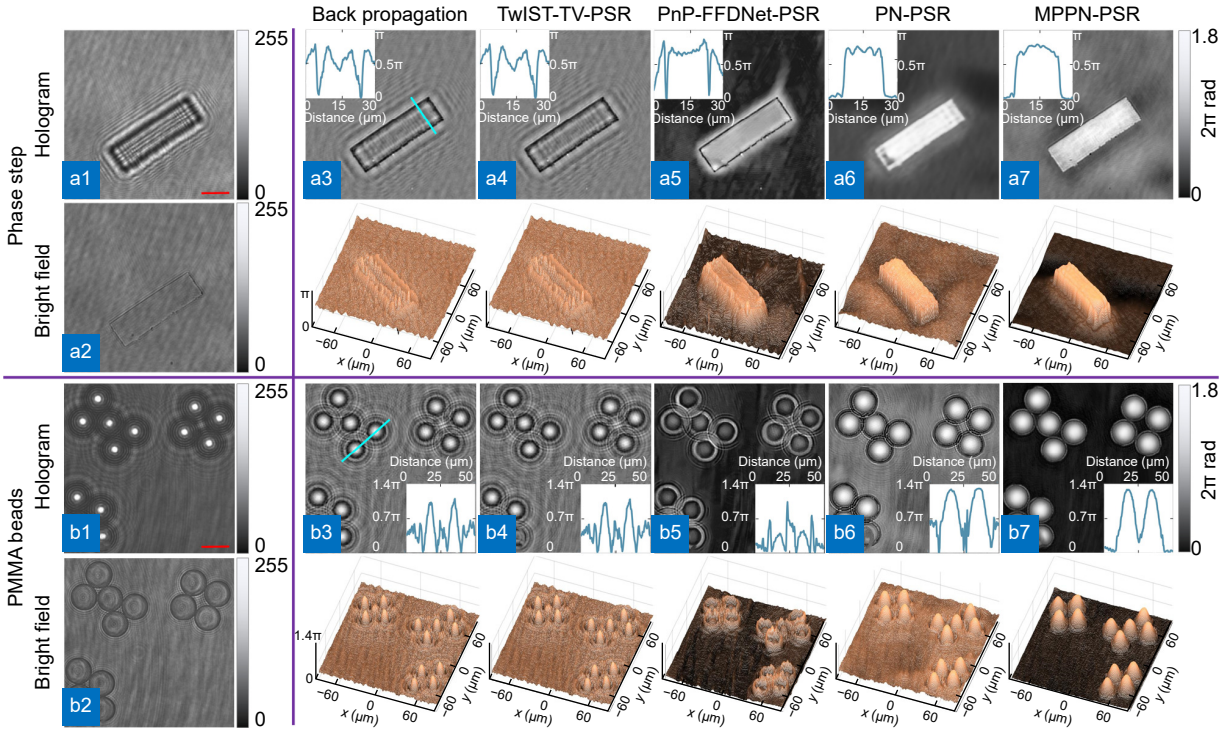

Fig. 9 | Experimental images of the phase step (**a1**–**a7**) and PMMA beads (**b1**–**b7**) processed with back propagation, TwIST-TV-PSR, PnP-FFD-Net-PSR, PN-PSR, and MPPN-PSR methods, respectively. The down-sampling rate is θ = 3, consistent with all subsequent experiments. The cross-section phase profiles (along the blue lines) were also measured in insets and the corresponding optical thickness maps are shown. The reconstruction size is 1200×1200 pixels, corresponding to the FOV of 130×130 μm². The red scale bar measures 20 μm.

understanding and comparison with the phase results. Based on the above performance analysis, θ = 3 was utilized in all experiments. The results were uniformly normalized, to investigate imaging contrast and background smoothness ability. Compared with the other methods, both the profiles along the blue lines and the 3D view of the reconstructed results from MPPN-PSR are more consistent with the actual situation. Not only clear display of more details and lower background noise shows the advantages of the proposed MPPN-PSR

method in quantitative phase imaging with pixel super-resolution, twin-image, and noise suppression. An exciting phenomenon worth noting is the inevitable occurrence of speckle noise in experiments, reflected in holograms and bright field images. MPPN-PSR treats it as noise and eliminates it together. The averaged phase value of the phase step calculated according to the envelope curve is $\varphi = 0.824\pi$ rad, corresponding to a thick of $h = \lambda\varphi/2\pi(n-1) = 619.45$ nm, which is consistent with actual value. The material of the phase step is SiO_2 and its refractive index (RI) is $n = 1.4556$[33], while the RI of around air medium is 1. The PMMA beads were immersed in a glycerol medium, the averaged maximum phase value of PMMA beads calculated according to the envelope curve is $\varphi = 1.678\pi$ rad, corresponding to a height of $h = \lambda\varphi/2\pi(n-n_0) = 20.165$ μm, which is also in agreement with the nominal value of 20 μm. The RI of PMMA beads is $n = 1.4969$, and that of glycerol is $n_0 = 1.4684$[33]. This experiment proves the MPPN-PSR method has high reliability in the phase reconstruct from a single-shot DIHM hologram.

The imaging experiments were further conducted on biological specimens including butterfly wing, fish ovary, TOMM20 antibody and frog intestine. The recorded holograms and reconstructed phases from different methods are shown in Figs. 10 and 11. The results demonstrate that the proposed method can achieve pixel super-resolution and suppress twin-images effectively. Specifically, as shown in Fig. 10(a), the fine structure of butterfly wings, both ridges along the longitudinal length of the scales and cross ribs connecting these ridges[34], can be observed in the reconstructed phase of Fig. 10(a7) using the MPPN-PSR method. In contrast, only the ridges can be observed with other methods in Fig. 10(a3–a6) due to the limited resolution. Similarly, the ovary cell boundaries are more easily distinguished using the proposed method as shown in Fig. 10(b7), where the fluctuations of the envelope curve reveal more details about the cells due to the pixel super-resolution reconstruction. Moreover, MPPN-PSR exhibits stronger imaging contrast and better background smoothness compared with other reconstructions in Fig. 11. This is more pronounced in the corresponding optical thickness distribution display, with the background closer to 0 rad but more prominent and clearer phase information of targets compared with other reconstructions. All of them prove the excellent twin-image and noise suppression ability of the MPPN-PSR.

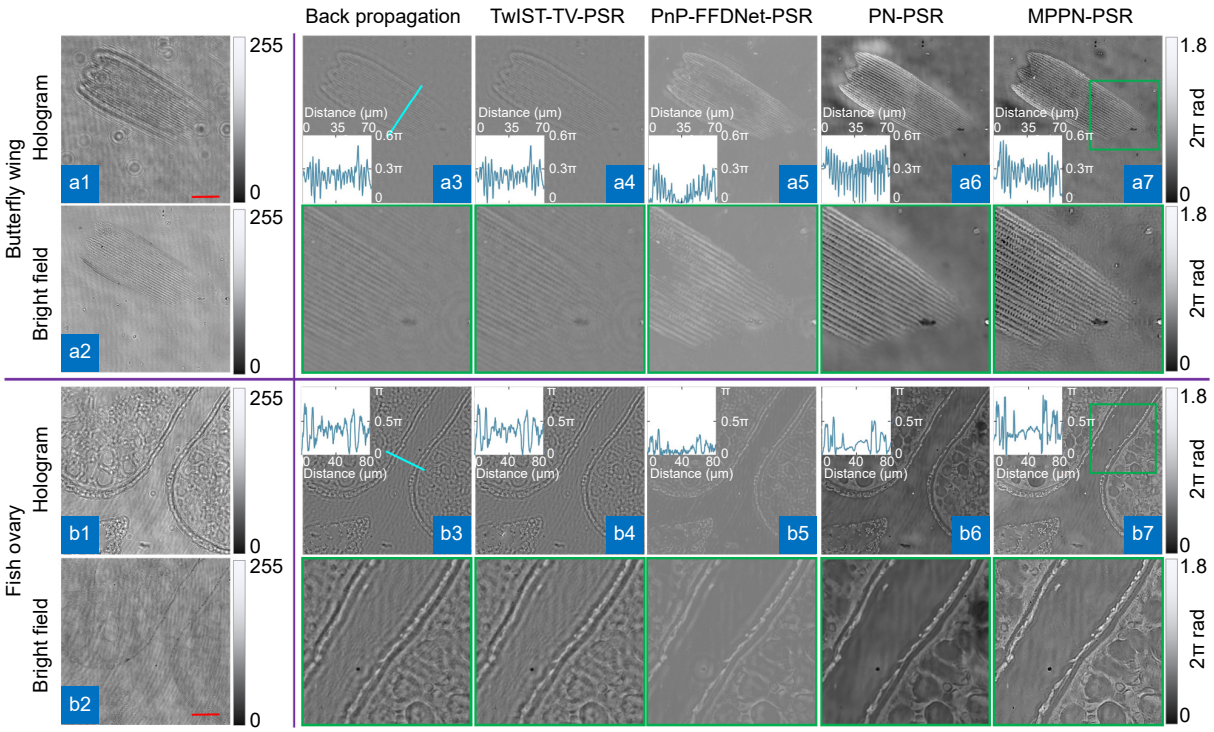

Fig. 10 | Imaging results of (**a**) butterfly wing and (**b**) fish ovary with different methods, including the reconstructed phase maps and the magnified views of selected regions. The reconstruction size is 1536 × 1536 pixels, i.e. $\theta = 3$, corresponding to the FOV of 166×166 μm². The red scale bar measures 25 μm.

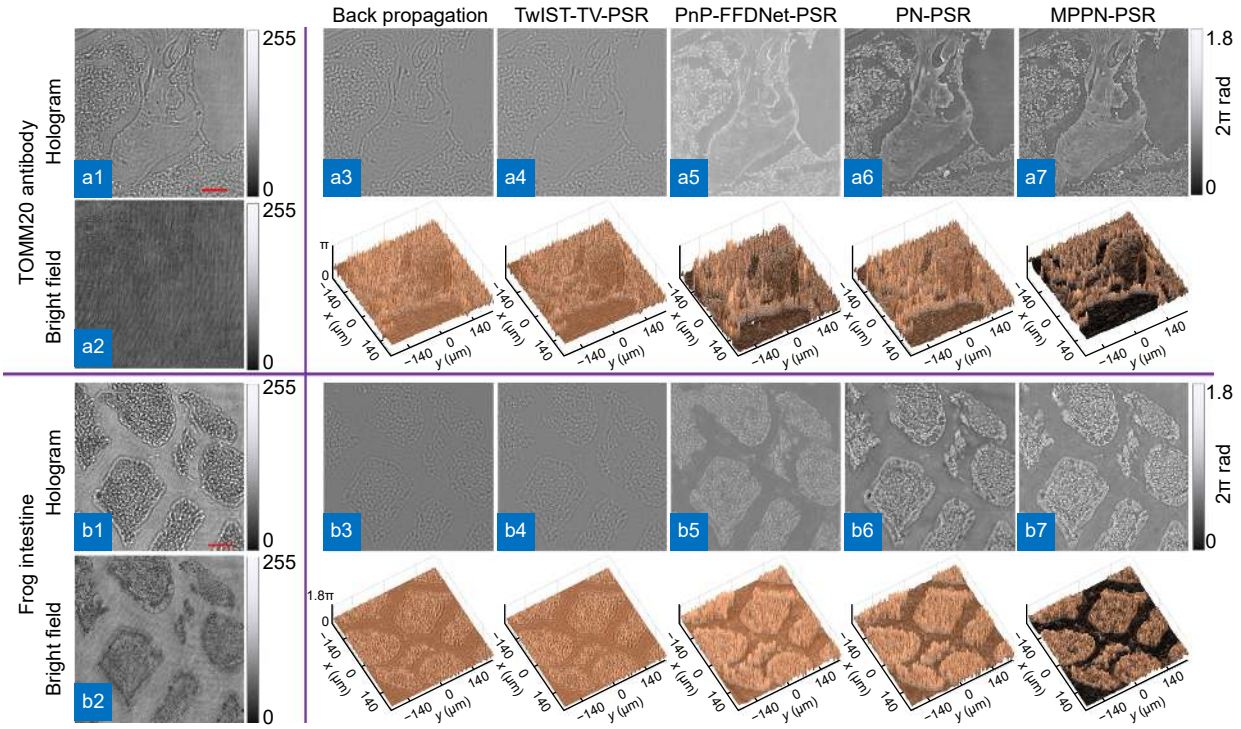

Fig. 11 | Imaging results of (**a**) TOMM20 antibody and (**b**) frog intestine by different methods. The reconstruction size is 2700 × 2700 pixels, i.e. θ=3, corresponding to the FOV of 293×293 μm². The red scale bar measures 40 μm.

In addition, the NPBMs are summarized and presented in Table 3. An averaged NPBM of MPPN-PSR reaches about 0.23, representing MPPN-PSR can provide more accurate edge information, richer texture structure, and higher frequency components of phase maps. Furthermore, the signal-to-noise ratio (SNR) was investigated to quantitatively assess the reconstruction results and focus more on measuring the noise level[31], which is also summarized in Table 3. Similar to the performance change trend obtained from NPBM analysis, with occupying the best-average SNR of above 40 dB, the results validate the MPPN-PSR method is competent for phase retrieval in the presence of sub-pixel information loss, the twin-image, and other experimental noises including the speckle noise and the shot noise. Moreover, in terms of the resolution, the autocorrelation functions corresponding to the magnified view in Fig. 10 are shown in Fig. 12, wherein it can be observed that the main lobe of the MPPN-PSR is narrower than other lobes. The FWHM of each lobe in Fig. 12 was measured, and the averaged value of MPPN-PSR can reach to a resolution enhancement of about 2.26-fold than that of TwIST-TV-PSR, which is consistent with the simulation.

High-throughput quantitative phase imaging

We further demonstrate the full-field high-resolution phase recovery from experimentally acquired intensity images of the quantitative phase target using MPPN-PSR through a 10× objective lens (*NA* = 0.25, Nikon Inc., Japan). As can be seen in Fig. 13(a) and 13(b), the low-resolution (LR) hologram suffers from the loss of sub-pixel information, where the high-frequency components almost completely disappear in the extremely low contrast and oversized pixels. With the LR hologram as

Table 3 | Quantitative results of NPBM/SNR of different methods[②].

NPBM/SNR (dB)	Back propagation	TwIST-TV-PSR	PnP-FFDNet-PSR	PN-PSR	MPPN-PSR
Butterfly wing	0.43/18.24	0.42/25.01	0.34/26.99	0.28/31.37	**0.21/39.94**
Fish ovary	0.41/16.33	0.37/16.70	0.36/17.50	0.31/23.16	**0.24/41.11**
TOMM20 antibody	0.43/28.00	0.36/31.32	0.36/32.89	0.29/35.66	**0.22/46.10**
Frog intestine	0.38/23.56	0.38/24.84	0.37/26.17	0.31/30.71	**0.21/38.64**

[②]The NPBM ranges from 0 to 1 (lower is better).

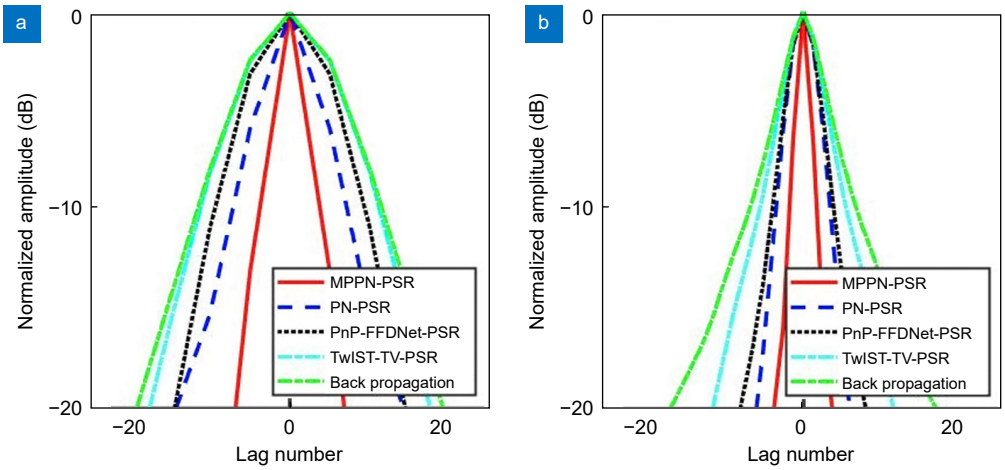

Fig. 12 | The autocorrelation functions of (**a**) butterfly wing and (**b**) fish ovary with different methods.

input, TwIST-TV-PSR and PN-PSR could provide phase images with relatively enhanced resolution (Fig. 13(a)), but still create a great obstacle to the observation of the detailed structure. In contrast, MPPN-PSR has a minimum requirement and possesses PSR capability. With a single frame of LR hologram as the only input, MPPN-PSR generates the PSR phase image with 5700×5700 pixels (Fig. 13(b)), achieving 3-fold expansion in pixel number. As shown in three enlarged ROIs in Fig. 13(d) and their corresponding bright field images in Fig. 13(c), MPPN-PSR enables the precise observation of plentiful features of the phase target, such as the profiles along the blue line marked on the 6-th element of the 8-th group. In contrast, TwIST-TV-PSR only resolves the features of the 6-th element at the 7-th group, representing that the optical resolution can reach a 2-fold enhancement. Although PN-PSR appears to have extent resolution, by measuring the cross-sectional envelope along the orange-colored line, the peak-to-peak value also indicates that the contrast of MPPN-PSR is about 2.78 times higher than that of PN-PSR, indicating that MPPN-PSR has better background and noises suppression ability. With showcasing more details, MPPN-PSR improves the resolution without sacrificing FOV, enhancing the throughput of the system effectively. In addition, the results of cascading non-PSR reconstruction with outstanding pixel super-resolution networks, i.e. state-of-art BSRGAN and BSRNet[35], have also been demonstrated, although this approach represents over-smooth and artifacts.

We also verified the feasibility of MPPN-PSR to achieve high throughput single-shot DIHM for a biological sample. Figure 14 shows the full FOV phase prediction for the sample of TOMM20 antibody. The input LR hologram has a wide FOV of about 1.37 mm^2, matching the FOV size of the objective lens with 10× magnification. The input intensity image has a resolution of 1800 × 1800 pixels with a pixel size of 6.5 × 6.5 μm^2. The high-throughput phase reconstruction is displayed in Fig. 14(a), which shows that our MPPN-PSR is able to achieve a 3-fold enhancement in the pixel number from 1800 × 1800 pixels to 5400 × 5400 pixels while maintaining the large FOV size of 1.17 × 1.17 mm^2, as the effective pixel size improves to 2.17 × 2.17 μm^2. The comparison between the predicted phase of two ROIs is shown in Fig. 14(b), accompanied with corresponding optical thickness maps in Fig. 14(c). The recovered phases display improved overall contrast of cell structures and highlight high-spatial-frequency cellular details. Similarly, BSRGAN and BSRNet networks introduce unsatisfactory over-smooth and artifacts with non PSR reconstruction. These experimental results validate the efficacy and promptness of the MPPN-PSR utilization within a DIHM microscopy system.

All these imaging results and analyses show that compared with the MPPN-PSR approach, other methods cannot produce enough fine detail and completely suppress the twin-image due to the limited resolution and noise effects. It is also found that the TwIST-TV-PSR method is usually ineffective when facing the requirements of pixel super-resolution and noise suppression simultaneously, whereas the PnP-FFDNet-PSR method produces over-smoothed results under the strong noise conditions. On the contrary, with the assistance of sparsity constraint, ℓ-1 regularization and a physical propagation model, the phase reconstruction of MPPN-PSR can achieve the best results, and converge faster than

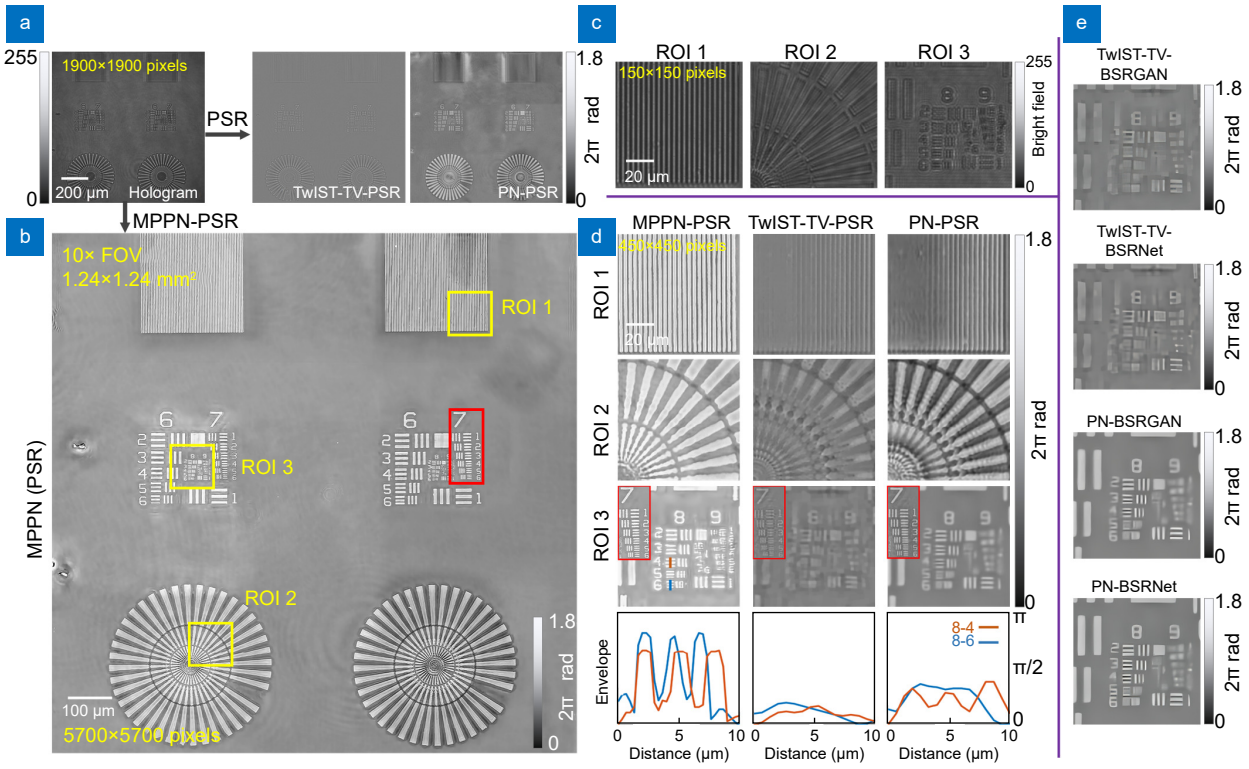

Fig. 13 | The experimental result of MPPN-PSR to reconstruct the full-FOV high-resolution phase image of a quantitative phase target. (**a**) The full-FOV LR defocused hologram, and the phase image reconstructed by TwIST-TV-PSR and PN-PSR. (**b**) The full-FOV PSR phase image reconstructed by MPPN-PSR from a single frame of LR hologram. (**c**) The LR bright field images of three ROIs. (**d**) The phase images of the three ROIs reconstructed by MPPN-PSR, TwIST-TV-PSR and PN-PSR, respectively. (**e**) The results of cascading non-PSR reconstruction with outstanding pixel super-resolution networks, i.e. BSRGAN and BSRNet, have also been demonstrated, although this approach represents over-smooth and artifacts. The profiles along the blue and orange-colored lines are also investigated.

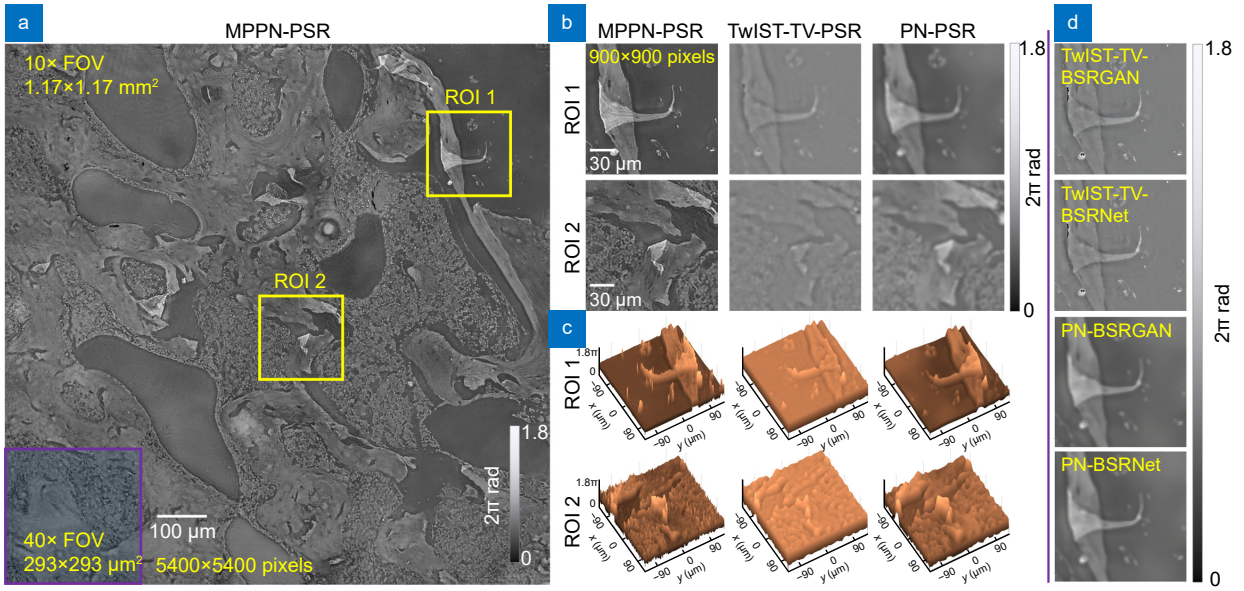

Fig. 14 | (**a**) The full-FOV PSR phase reconstruction of the TOMM20 antibody by MPPN-PSR, (**b**) and the comparison of PSR phase images of two ROIs. (**c**) The corresponding optical thickness maps are shown as well. (**d**) BSRGAN and BSRNet networks introduce unsatisfactory artifacts with non PSR reconstruction as well. The purple area represents the FOV that a 40× objective lens can bring.

PN-PSR. For MPPN-PSR, the specific parameters of imaging have been integrated into the forward physical model, including wavelength, pixel size of camera, down-sampling rate, diffraction distance, etc. When the experimental conditions change, we only need to adjust the parameters in the forward model accordingly to obtain the corresponding pixel super-resolution outputs, which is also very convenient and meets the imaging rules in practical utilization. Besides, no additional requirements are imposed on either the method of data acquisition or the illumination conditions. Both simulation and real-world data captured by experiments have verified the outperformance of MPPN-PSR scheme. However, current MPPN-PSR does not perform well for phase modulation ranges larger than 2π. In other words, the phase unwrapping problem is not focused and investigated in this study, which should be explored in future research.

Conclusion

In terms of DIHM, high-throughput imaging faces two major obstacles posed by sub-pixel information loss and twin-image problem. In optical systems, detectors are used to collect intensity information and are typically designed with large pixel sizes to accommodate high photosensitivity and large FOVs for high-throughput imaging. However, large pixel sizes may lead to inadequate sampling or digitization of the transmitted intensity, resulting in low pixel resolution and even leading to the infamous under-sampling problem. The sub-optimal use of spatial bandwidth product (SBP) in imaging systems leads to a trade-off between pixel resolution and FOV. For another, while some holographic setups capable of eliminating the twin-image have been presented, they add complexity to the recording process. In this study, a novel deep learning-based technique of MPPN-PSR is introduced for phase retrieval with pixel super-resolution, twin-image-free and noise insensitive capability. This technique encapsulates the physical model prior, the sparsity prior and the deep image prior into an untrained deep neural network. The physical model prior represents the DIHM imaging process and down-sampling of the detector, while the sparsity prior further enhances the imaging resolution. The performance of the proposed MPPN-PSR method was evaluated and compared with other retrieval methods by using the metrics such as SSIM, PSNR, NPBM, *etc.*, to quantitatively analyze the imaging results. Through the MPPN-PSR, the pixel resolution of phase imaging can be increased by 3 times compared with phase retrieval without PSR, while the optical resolution can be improved by about 2 times compared to TwIST-TV-PSR. Given its capability of achieving quantitative phase imaging with pixel super-resolution, twin-image-free and high-throughput from single-shot hologram over conventional DIHM microscope hardware, the proposed approach is expected to be widely adopted in biomedical workflow and industrial measurement.

References

1. Kemper B, von Bally G. Digital holographic microscopy for live cell applications and technical inspection. *Appl Opt* **47**, A52–A61 (2008).
2. Schnars U, Jüptner WPO. Digital recording and numerical reconstruction of holograms. *Meas Sci Technol* **13**, R85–R101 (2002).
3. Garcia-Sucerquia J, Xu WB, Jericho SK et al. Digital in-line holographic microscopy. *Appl Opt* **45**, 836–850 (2006).
4. Zhou J, Jin YB, Lu LP et al. Deep learning-enabled pixel-super-resolved quantitative phase microscopy from single-shot aliased intensity measurement. *Laser Photonics Rev* **18**, 2300488 (2024).
5. de Almeida JL, Comunello E, Sobieranski A et al. Twin-image suppression in digital in-line holography based on wave-front filtering. *Pattern Anal Appl* **24**, 907–914 (2021).
6. Bai C, Peng T, Min JW et al. Dual-wavelength in-line digital holography with untrained deep neural networks. *Photonics Res* **9**, 2501–2510 (2021).
7. Zhang JL, Sun JS, Chen Q et al. Adaptive pixel-super-resolved lensfree in-line digital holography for wide-field on-chip microscopy. *Sci Rep* **7**, 11777 (2017).
8. Luo W, Zhang YB, Feizi A et al. Pixel super-resolution using wavelength scanning. *Light Sci Appl* **5**, e16060 (2016).
9. Pellizzari CJ, Spencer MF, Bouman CA. Coherent plug-and-play: digital holographic imaging through atmospheric turbulence using model-based iterative reconstruction and convolutional neural networks. *IEEE Trans Comput Imag* **6**, 1607–1621 (2020).
10. Chang XY, Bian LH, Gao YH et al. Plug-and-play pixel super-resolution phase retrieval for digital holography. *Opt Lett* **47**, 2658–2661 (2022).
11. Bao P, Situ GH, Pedrini G et al. Lensless phase microscopy using phase retrieval with multiple illumination wavelengths. *Appl Opt* **51**, 5486–5494 (2012).
12. Luo W, Greenbaum A, Zhang YB et al. Synthetic aperture-based on-chip microscopy. *Light Sci Appl* **4**, e261 (2015).
13. Yamaguchi I, Zhang T. Phase-shifting digital holography. *Opt Lett* **22**, 1268–1270 (1997).
14. Song J, Swisher CL, Im H et al. Sparsity-based pixel super resolution for lens-free digital in-line holography. *Sci Rep* **6**, 24681 (2016).
15. Raupach SMF. Cascaded adaptive-mask algorithm for twin-image removal and its application to digital holograms of ice crystals. *Appl Opt* **48**, 287–301 (2009).
16. Zhang WH, Cao LC, Brady DJ et al. Twin-image-free holography: A compressive sensing approach. *Phys Rev Lett* **121**,

093902 (2018).
17. Gao YH, Cao LC. Generalized optimization framework for pixel super-resolution imaging in digital holography. *Opt Express* **29**, 28805–28823 (2021).
18. Wang H, Lyu M, Situ GH. eHoloNet: A learning-based end-to-end approach for in-line digital holographic reconstruction. *Opt Express* **26**, 22603–22614 (2018).
19. Rivenson Y, Zhang YB, Günaydın H et al. Phase recovery and holographic image reconstruction using deep learning in neural networks. *Light Sci Appl* **7**, 17141 (2018).
20. Lempitsky V, Vedaldi A, Ulyanov D. Deep image prior. In *2018 IEEE/CVF Conference on Computer Vision and Pattern Recognition* 9446–9454 (IEEE, 2018); http://doi.org/10.1109/CVPR.2018.00984.
21. Wang F, Bian YM, Wang HC et al. Phase imaging with an untrained neural network. *Light Sci Appl* **9**, 77 (2020).
22. Han F, Mu TK, Li HY et al. Deep image prior plus sparsity prior: Toward single-shot full-stokes spectropolarimetric imaging with a multiple-order retarder. *Adv Photonics* **2**, 036009 (2023).
23. Galande AS, Thapa V, Gurram HPR et al. Untrained deep network powered with explicit denoiser for phase recovery in inline holography. *Appl Phys Lett* **122**, 133701 (2023).
24. Niknam F, Qazvini H, Latifi H. Holographic optical field recovery using a regularized untrained deep decoder network. *Sci Rep* **11**, 10903 (2021).
25. Mait JN, Euliss GW, Athale RA. Computational imaging. *Adv Opt Photonics* **10**, 409–483 (2018).
26. Zhao WS, Zhao SQ, Li LJ et al. Sparse deconvolution improves the resolution of live-cell super-resolution fluorescence microscopy. *Nat Biotechnol* **40**, 606–617 (2022).
27. Zhao H, Gallo O, Frosio I et al. Loss functions for image restoration with neural networks. *IEEE Trans Comput Imag* **3**, 47–57 (2017).
28. Ravishankar S, Ye JC, Fessler JA. Image reconstruction: from sparsity to data-adaptive methods and machine learning. *Proc IEEE* **108**, 86–109 (2020).
29. Ronneberger O, Fischer P, Brox T. U-net: convolutional networks for biomedical image segmentation. In *Proceedings of the 18th International Conference on Medical Image Computing and Computer-Assisted Intervention* 234–241 (Springer, 2015); http://doi.org/10.1007/978-3-319-24574-4_28.
30. Schanz D, Gesemann S, Schröder A et al. Non-uniform optical transfer functions in particle imaging: Calibration and application to tomographic reconstruction. *Meas Sci Technol* **24**, 024009 (2013).
31. Bai C, Liu C, Jia H et al. Compressed blind deconvolution and denoising for complementary beam subtraction light-sheet fluorescence microscopy. *IEEE Trans Biomed Eng* **66**, 2979–2989 (2019).
32. Crete F, Dolmiere T, Ladret P et al. The blur effect: Perception and estimation with a new no-reference perceptual blur metric. In *Proceedings of the SPIE 6492, Human Vision and Electronic Imaging XII* 64920I (SPIE, 2007); http://doi.org/10.1117/12.702790.
33. Polyanskiy MN. Refractiveindex. Info database of optical constants. *Sci Data* **11**, 94 (2024).
34. Luke SM, Vukusic P, Hallam B. Measuring and modelling optical scattering and the colour quality of white *pierid* butterfly scales. *Opt Express* **17**, 14729–14743 (2009).
35. Zhang K, Liang JY, Van Gool L et al. Designing a practical degradation model for deep blind image super-resolution. In *2021 IEEE/CVF International Conference on Computer Vision (ICCV)* 4771–4780 (IEEE, 2021); http://doi.org/10.1109/ICCV48922.2021.00475.

Acknowledgements

We are grateful for financial supports from National Natural Science Foundation of China (62275267, 62335018, 12127805, 62105359), National Key Research and Development Program of China (2021YFF0700303, 2022YFE0100700), and Youth Innovation Promotion Association, CAS (2021401).

Author contributions

T. Xuan and R. Z. Li proposed the original idea. C. Bai and B. L. Yao supervised the project. T Peng and Y. G. Xue fabricated the samples and performed the measurements. J. W. Min and X. Li discussed the interpretation of results. All authors discussed the results and commented on the manuscript.

Competing interests

The authors declare no competing financial interests.